Design of a circum-scanning light detection and ranging emission system

Naitao Xu,[a,*] Pangyue Li,[b,*] Shun Zhou,[a] Jin Cheng,[a] Xishun Peng,[c] Chen Fan,[a] Yanjie Lei,[b] Xinyan Zheng,[a] Jiahao Liu,[a] and Weiguo Liu[a,b]

[a]Xi'an Technological University, School of Optoelectronic Engineering, Xi'an, China
[b]Xi'an Technological University, School of Armament Science and Technology, Xi'an, China
[c]Guizhou University, College of Big Data and Information Engineering, Guizhou, China

Abstract. The need for imaging and detecting in various instrument areas has brought light detection and ranging (LiDAR) to the forefront of consumer technology. Among different LiDAR, microelectromechanical system (MEMS) LiDAR has more appeal due to its small size and high integration. However, due to its low resolution and slight scanning angle, MEMS LiDAR does not apply to all scenes. Thus we presented a 360-deg scanning LiDAR emission optical system. Design formulas were deduced from theoretical formulas. In this system, the aspheric lens collimated the beam, MEMS micromirrors tracked the concentric circular beams, and the converging lens compensated for the divergence of the outgoing beam. By doing so, the target was scanned 360 deg at high resolution. With Zemax, the fast-axis divergence angle was 0.2484 mrad, the slow-axis divergence angle was 0.1546 mrad, and the system energy utilization rate was 84.16% with an angular resolution of 0.0142 deg at a distance of 10,000 mm. We have provided a potential solution for improving the scanning angle and resolution of MEMS LiDAR.
 [DOI: 10.1117/1.OE.62.3.035101]

Keywords: microelectromechanical system (MEMS) light detection and ranging; aspheric lens; MEMS micromirrors; converging lens; optical design.

Paper 20221354G received Nov. 17, 2022; accepted for publication Feb. 14, 2023; published online Mar. 11, 2023.

1 Introduction

Light detection and ranging (LiDAR) is a crucial player in the growing field of photoelectric detection.[1] Since it was first proposed in 1970 by NASA, LiDAR has achieved significant advances with high detection accuracy, fast response speed, long working distances, and strong anti-interference ability. Numerous applications have been proposed for LiDAR, ranging from aerospace and uncrewed vehicles to precision positioning and laser guidance.[2–4] Depending on the scanning technique, LiDAR can be classified as a hybrid solid-state LiDAR, mechanical scanning LiDAR, or an all-solid-state LiDAR. Microelectromechanical system (MEMS) LiDAR, also commonly known as hybrid solid-state LiDAR, offers many advantages over traditional LiDAR technology with low cost, small size, and high integration of MEMS micromirrors as its core.[5,6] By doing so, it can effectively figure out the problems of large volumes and complex optical systems, providing a new solution for LiDAR applications.

With MEMS micromirrors, MEMS LiDAR can precisely regulate frequency and field of view.[7] However, MEMS micromirrors have slight scanning angles, typically 10 deg to 15 deg, making them unsuitable for applications requiring wide scanning angles. Research has been conducted on this problem by both domestic and foreign researchers, and various solutions have been proposed. In Toyota Central R&D Labs, three laser diodes were arranged into a linear array on MEMS micromirrors, which could extend optical scanning angles by three times.[8] The downside of this scheme was that it involved many laser diodes, making it relatively expensive and not conducive to miniaturizing LiDAR systems. Lee[9] (Harbin Institute of Technology) suggested

*Address all correspondence to Naitao Xu, xunaitao_123@163.com; Pangyue Li, lpy971230@163.com

combining positive and negative lens groups for expanding scanning angles. This scheme utilized a positive and a negative lens for collimating and expanding beams, which yielded an optical scanning angle above 60 deg. However, it had several disadvantages, including a high divergence angle for the exit beam, a low system resolution, and an inability to detect long distances. The Dutch company Innoluce, working with its partner Osram, has developed a prototype LiDAR that used MEMS technology for beam reflection to simulate the scanning LiDAR principle. With a resolution of 0.1 deg, the LiDAR system could view 120 deg.[10] It is remarkable that the above teams have achieved some results in extending the scanning angle of MEMS LiDAR. Despite this, the LiDAR system's complexity and high volume and low resolution still need to be addressed. Consequently, this paper proposed a MEMS LiDAR emission optical system capable of 360-deg scanning to overcome this issue.

In this system, the light source produced the beam calibrated by an aspheric lens before the incident on the MEMS micromirrors. Then MEMS micromirrors scanned concentric circles and projected them into the spherical mirrors. Finally, the beam exited the system in a horizontal direction after being reflected by the spherical mirror. Due to its simple optical structures and high resolution, the circum-scanning LiDAR emission optical system has many advantages over comparable methods.

2 Principle of the Circum-Scanning LiDAR System

2.1 *System Scenario*

As illustrated in Fig. 1, an overview of the circum-scanning LiDAR emission optical system is presented. This system has five main components: a light source, an aspheric lens, MEMS micromirrors, a converging lens, and a spherical mirror. The light source is an infrared-pulsed semiconductor laser near 905 nm, which simulates LiDAR's actual operating conditions more accurately. The new rotating MEMS scanning micromirrors, which our team has independently developed, are capable of scanning concentric circular beams in two dimensions. It is possible to collimate semiconductor laser beams using an aspheric lens. Combining spherical mirrors and rotating MEMS scanning micromirrors makes 360-deg scanning possible. A converging lens is added in front of the spherical mirror to compensate for the divergence of the angle of the outgoing beam.

Followings are the steps involved in the system: with the aspheric lens, the Gaussian beam output from the 905-nm semiconductor laser is collimated and projected onto the MEMS micromirrors. MEMS micromirrors then scan the beams as concentric circles. In addition, the beam passes through the converging lens and is reflected by the spherical mirror before exiting horizontally.

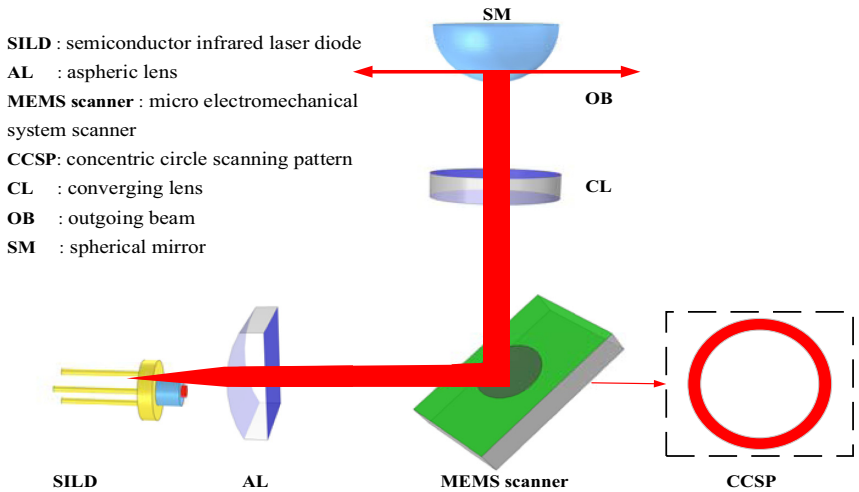

Fig. 1 Schematic diagram of the circum-scanning LiDAR emission optical system.

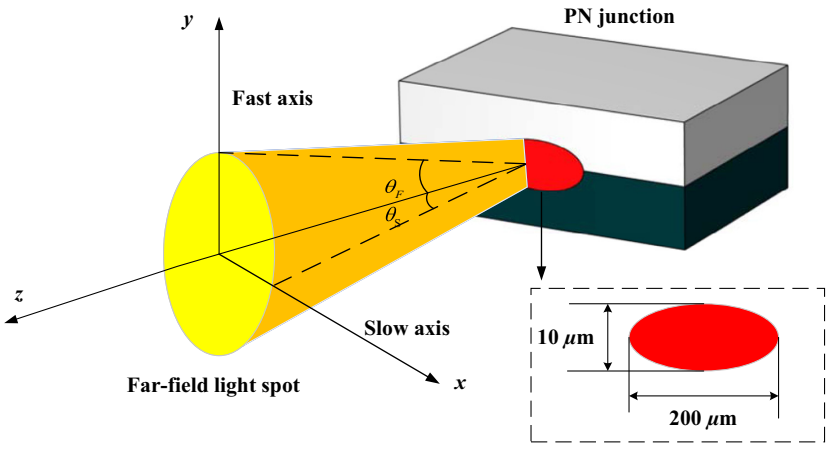

Fig. 2 An illustration of semiconductor laser structure.

2.2 *Characteristics of Semiconductor Lasers*

According to Fig. 2, a semiconductor laser's structure and emission beam are shown schematically. In Fig. 2, the x direction is perpendicular to the plane of the P–N junction (slow axis), the y direction is parallel to the plane of the P–N junction (fast axis), and the z direction is the optical axis. Typically, semiconductor lasers have an aspect ratio of 100:1 for their rectangular active region.[11] The semiconductor laser has a thickness of 10 mm on the y axis and 200 mm on the x axis. As the divergence velocity of a semiconductor laser varies inversely with its thickness and width, a larger beam divergence angle is present in the y direction compared with a smaller beam divergence angle in the x direction. Due to this, the laser produces an elliptical spot in the far field with the major axis in the y direction.

The output beam of a semiconductor laser follows a Gaussian light distribution in both the fast and slow axes.[12] It is possible to calculate the intensity distribution of the laser's light-emitting unit as follows:

$$I(\theta_x, \theta_y) = I_0 \exp\left\{-2\left[\left(\frac{\theta_x}{\theta_S}\right)^{2G_x} + \left(\frac{\theta_y}{\theta_F}\right)^{2G_y}\right]\right\}, \tag{1}$$

where I_0 is the intensity of light along the z axis, θ_S is the divergence angle of the slow axis, θ_F is the divergence angle of the fast axis, θ_x is the angle between the beam and the $x-z$ plane, θ_y is the angle between the beam and the $y-z$ plane, and G_x and G_y are defined as ultra-Gaussian factors in the x and y directions, respectively.

2.3 *Design of Aspheric Lenses*

2.3.1 *Determination of surface parameters*

Considering that semiconductor lasers have different divergence angles, an output spot cannot be used directly, causing the laser output beam to be shaped. In the current state of research, beam shaping methods include microlens array,[13] freeform lens,[14] diffractive optical elements,[15] telescope, and aspheric lens.[16,17] Considering the aspheric lens's minimal size, simplicity, and slight energy loss, it is preferred for shaping semiconductor laser beams. This paper uses a single aspheric lens to align beams simultaneously in the fast and slow axes, and different surface shape parameters are designed for each. Fast-axis collimation is performed on the first surface, and slow-axis collimation is performed on the second surface. The design principles of each are illustrated in Figs. 3 and 4.

As illustrated in Fig. 3, luminary A, which is at the focal length of the first side of the aspheric lens in the $y-z$ plane, is considered an ideal point of light. As the spherical beam yields from point A, it strikes the front surface of the aspheric lens S_1, passes through S_1, and exits parallel to the optical axis. Fermat's principle[18] states that the optical path travelled by a beam from point A

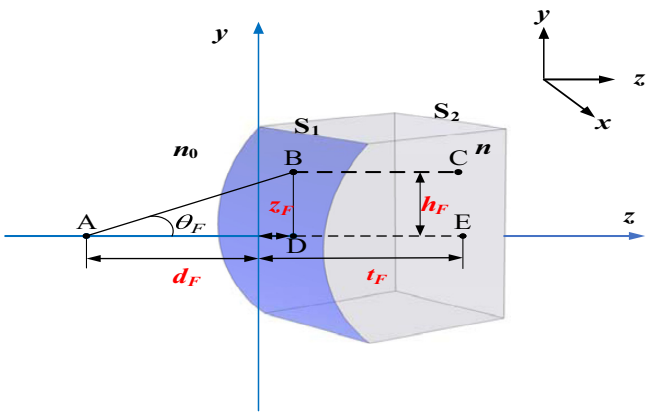

Fig. 3 Scenario for collimating the beam of an aspheric lens in the fast axis.

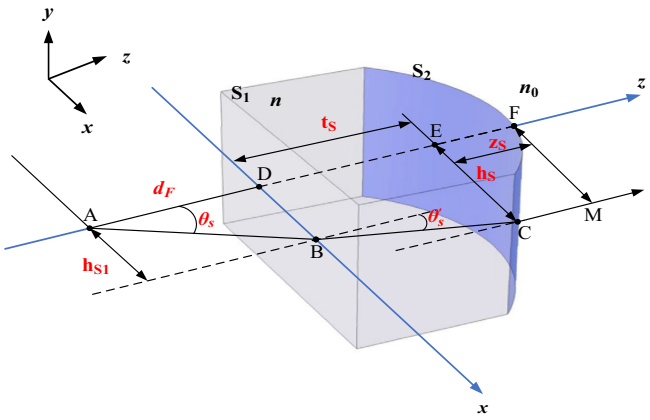

Fig. 4 Scenario for collimating the beam of an aspheric lens in the slow axis.

to the point outside the axis equals the way travelled from the point on the axis to the point outside of it. It means that $L_{AB} + L_{BC} = L_{AD} + L_{DE}$ (L represents the optical path). The aplanatic equation is as follows:

$$n_0 \cdot d_F + n \cdot t_F = n_0 \cdot \sqrt{h_F^2 + (d_F + z_F^2)} + n \cdot (t_F + z_F), \tag{2}$$

where n_0 represents the refractive index of air at one as a general rule, n is the refractive index of the materials for the aspheric lens, d_F is the focal length of the aspheric lens's front surface, t_F is the thickness of the aspheric lens, and h_F is defined as the height in which the beam is incident on the front surface. Taking z_F into account in Eq. (2), the following expression can be obtained

$$z_F(h_F) = \frac{\frac{1}{d_F(n-1)} \cdot h_F^2}{1 + \sqrt{1 - (1 - n^2) \cdot \left(\frac{1}{d_F^2(n-1)^2}\right) \cdot h_F^2}}. \tag{3}$$

Aspheric design theory states that rotationally symmetric even-degree aspheric equations are expressed as follows:

$$z = \frac{c \cdot r^2}{1 + \sqrt{1 - (1 + k) \cdot c^2 \cdot r^2}} + \sum_{i=1}^{n} a_{2i} r^{2i}. \tag{4}$$

In Eq. (4), c is the reciprocal radius of curvature, k is referred to the conic coefficient of the aspheric surface, and $\sum_{i=1}^{n} a_{2i} r^{2i}$ represents the multiple terms in the equation of the aspheric

surface. Comparing Eq. (3) with Eq. (4), a quadric surface type can be determined for the aspheric lens. Furthermore, it is possible to decide on the main parameters of the aspheric design: the radius of curvature R_F and its conic coefficient K_F. Its representation is as follows:

$$\begin{cases} R_F = d_F \cdot (n-1) \\ K_F = -n^2 \end{cases}. \tag{5}$$

With Eq. (6), we can calculate the focal length of an aspheric lens d_F, whereas $\tan(\theta_F)$ represents the angle of semidivergence of the fast axis. In Eqs. (5) and (6), all parameters of the fast-axis aspheric lens can be determined

$$d_F = \frac{\sqrt{h_F^2 + \left[\frac{h_F}{\tan(\theta_F)}\right]^2} - n \cdot \frac{h_F}{\tan(\theta_F)}}{1-n}. \tag{6}$$

Figure 4 shows the situation when the spherical beam emitted by luminary A hits the back surface of the aspheric lens S_2, and it is fired in parallel after convergence on that surface.

According to Fermat's principle, we can see that when a beam travels from point A to point outside the axis, it follows the same path as if it travelled from the point on the axis to the point outside. As illustrated in Fig. 4, $L_{\mathrm{AD}} + L_{\mathrm{DE}} + L_{\mathrm{EF}} = L_{\mathrm{AB}} + L_{\mathrm{BC}} + L_{\mathrm{CM}}$. Here is the aplanatic equation

$$n_0 \cdot \sqrt{d_F^2 + h_{s1}^2} + n \cdot \sqrt{t_s^2 + (h_s - h_{s1})^2} + n_0 \cdot z_s = n_0 \cdot d_F + n \cdot (t_s + z_s), \tag{7}$$

where h_{s1} represents the height in which the slow-axis beam strikes the S_1 surface and h_s is the height in which the slow-axis strikes the S_2 surface. It can be determined that the surface type of the aspheric lens in the slow-axis direction is quadric, following the same beam collimation principle as for the fast axis. In addition, the radius of curvature R_s and its conic coefficient K_s can be calculated by

$$\begin{cases} R_s = d_s \cdot (n-1) \\ K_s = -n^2 \end{cases}. \tag{8}$$

In Eq. (8), d_s represents the focal length of the back surface S_2, which can be calculated by

$$\begin{cases} d_s = \frac{\sqrt{h_{s_1}^2 + \left[\frac{h_{s_1}}{\tan(\theta_S)}\right]^2} - n \cdot \frac{h_s}{\tan(\theta_S)}}{1-n}, \\ h_{s_1} = d_F \cdot \tan(\theta_S) \end{cases} \tag{9}$$

where $\tan(\theta_S)$ represents the tangent to the half-divergence angle of the incident beam's fast axis. Currently, it is possible to determine all parameters concerning the type of aspheric surface in the slow-axis direction.

2.3.2 *Determination of the aspheric lens size*

Figure 5 depicts a geometric relationship between the spot size of the lens surface, the laser illuminating unit size, and the beam divergence angle. By determining the distance between the illuminating unit and the lens surface and the beam divergence angle, the spot diameters in each direction can be defined in Eq. (10). Factors, such as beam collection efficiency and optical system volume size, are comprehensively considered when it comes to the actual design process. It is possible to assure that light passing through an optical system is generally >98.8% of the total energy when the lens is three times larger than the spot size on the surface.[19] This way, we can determine the x and y dimensions of the aspheric lens:

$$\begin{cases} 2h_a = a + 2d_F \cdot \tan(\theta_F) \\ 2h_b = b + 2d_s \cdot \tan(\theta_S) \end{cases}, \tag{10}$$

where $2h_a$ and $2h_b$ are the spot diameters of the lens surface in x and y directions, respectively, and a and b are the length and width of the illuminating unit, respectively.

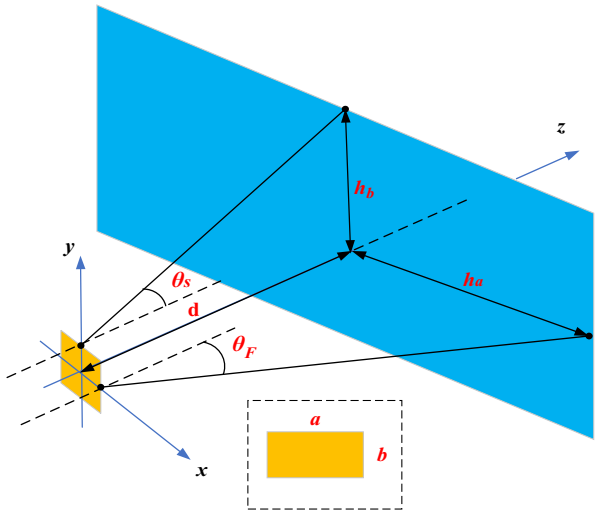

Fig. 5 An illustration of the luminous element versus the spot on the lens surface's size.

2.4 *Design of Converging Lens*

By collimating it with an aspheric lens and scanning it with MEMS micromirrors, the beam is reflected by the lens and emitted horizontally in 360 deg as it falls parallel to the spherical mirror. It is remarkable that a spherical mirror's normal direction varies with its position, causing the beam to exit divergent after reflection rather than parallel. Converging lenses are in front of the spherical mirror to compensate for outgoing beams to increase the angular resolution of the circum-scanning LiDAR emission system. Figure 6 shows the balanced optical path's optical principle.

This paper's design idea for compensating the outgoing beam is as follows: the beam's divergence angle after impacting the spherical mirror should be analyzed and calculated. After that, a converging lens is added to compensate for the optical path, making the parallel beam into a converged beam. The angle in which the beam converges equals the angle in which the beam diverges. The beam can maintain good collimation and high angular resolution in this design after leaving the spherical mirror.

Using the geometric and trigonometric relationship in the triangular ABO and the triangular BOD in Fig. 6, we can derive the following formula:

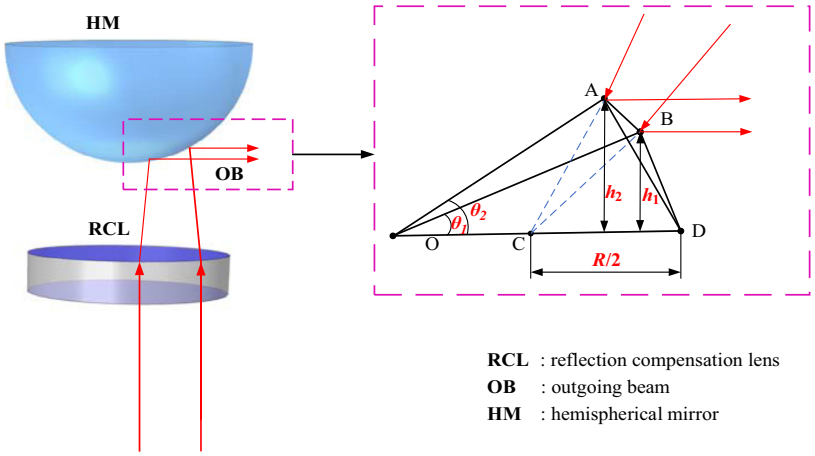

Fig. 6 An illustration of the compensation optical path's structure and principle.

$$\begin{cases} \sin(\theta_1) = \frac{h_1}{R} \\ \sin(\theta_2) = \frac{h_2}{R} \\ \cos(\theta_2) = \frac{\sqrt{R^2 - h_1^2}}{R} \\ \cos(\theta_2) = \frac{\sqrt{R^2 - h_2^2}}{R} \end{cases}, \tag{11}$$

where R is the radius of curvature of the spherical mirror, θ_1 and θ_2 represent the angle of incidence of two different beams, respectively, and h_1 and h_2 are the heights of the triangular AOD and triangular BOD, separately. In addition, the following equation can be drawn by applying the trigonometric and difference formulas:

$$\cos(\theta_2 - \theta_1) = \cos(\theta_2) \cdot \cos(\theta_2) + \sin(\theta_2) \cdot \sin(\theta_1) = \frac{h_1 h_2 + \sqrt{(R^2 - h_1^2)(R^2 - h_2^2)}}{R^2}. \tag{12}$$

In Eq. (12), the beam's convergence angle can be calculated using the inverse trigonometric function formula as follows:

$$\theta_2 - \theta_1 = \text{arc}\left(\frac{h_1 h_2 + \sqrt{(R^2 - h_1^2)(R^2 - h_2^2)}}{R^2}\right). \tag{13}$$

3 Zemax Implementation

3.1 *Design Specification*

This system was designed for 3D imaging LiDAR scanning with a wavelength of 905 nm, a reflective scanning type that can scan concentric beams by the new MEMS scanning micromirrors. Design goals for the system include the following: the maximum scanning angle can reach 360 deg, the angular resolution of the system is confined to 0.1 deg at a detection distance of 10,000 mm, and the energy utilization rate exceeds 80%.

3.2 *Design of the System*

The concentric circular beams scanned by the new rotating MEMS micromirrors were identical at each point. When a spherical mirror reflected the beam, the exit state of the beam remained the same at each point. As a convenience, we will only discuss a one-point case when designing the circum-scanning MEMS LiDAR emission optical system.

Five parts comprise the scanning system: a light source, an aspheric lens, MEMS micromirrors, a converging lens, and a spherical mirror. An aspheric lens produced a flattened beam from the Gaussian beam to illuminate the MEMS micromirrors' effective aperture effectively. The converging lens compensated for angular divergence caused by the spherical mirror when the beam passes through it. As a result of the theoretical analysis, we traced the rays using the standard optical design software Zemax, which offers features and tools to design, optimize, and analyze any optical system.

We used Zemax to simulate the circum-scanning LiDAR emission optical system. As a first step, we need to determine the light source. The light source used was an infrared-pulsed laser diode developed by OSRAM called SPLPL90-3. Furthermore, lens surface type parameters were determined using Eqs. (5)–(9), and lens size was determined by Eq. (10). In this way, the initial structure of the aspheric lens was yielded. Table 1 shows the parameters of the laser diode and the initial construction of the aspheric lens.

In accordance with the system's design indicators, an initial structure should be established. In the case of the aspheric lens, the radius of curvature and the lens thickness were variables, and they were optimized for luminous flux and Root Mean Square (RMS) x direction radius as target functions. Assess whether the optimized results met the design indicators. If not, add the conic coefficient of the aspheric lens as a variable and continue with optimization until it met the system's design specifications.

Table 1 Parameters of infrared-pulsed laser diodes and parameters of the initial structure of the aspheric lens.

Infrared-pulsed laser diode		Aspheric lens initial structure	
Parameter	Value	Parameter	Value
λ (nm)	905	Object type	Biconic lens
Power (W)	75	X-radius/μm	129.15
θ_F (deg)	25	Y-radius/μm	359.48
θ_S (deg)	9	Thickness/μm	450
G_x	1	R_{y1}	−251.91
G_y	1	K_{y1}	−2.2023
X width (μm)	10	R_{x2}	82.83
Y width (μm)	200	K_{x2}	−2.2023
—	—	Material	PMMA

Table 2 The structural parameters of optimized aspheric lens.

Parameter	X direction	Y direction
Aperture of lens (mm)	0.258	0.719
Thickness (mm)	0.524	0.524
Radius of the front surface (mm)	0.083	—
Radius of the back surface (mm)	—	−0.254
Conic of the front surface	−2.152	—
Conic of the back surface	—	−2.286

After optimizing the aspheric lens structure, Zemax added MEMS mirrors, compensation lenses, and spherical mirrors to the optical pathway. The diameter of the MEMS micromirrors was set to 5 mm, and the tilt angle was 45 deg. The converging lens, placed 100 mm behind the MEMS micromirrors, had an aperture of 20 mm and a thickness of 5 mm. Later, the overall structure of the system was determined. We optimized the converging lens by considering the luminous flux and RMS x direction. The structural parameters of the optimized aspheric lens were presented in Table 2. The structural parameters of the optimized converging lens and spherical mirrors are presented in Table 3.

Figure 7 illustrates the overall structure of the circum-scanning LiDAR emission optical system and the effect of beam collimation and compensation after Zemax implementation.

Table 3 The structural parameters of optimized converging lens and spherical mirrors.

Parameter	Converging lens	Spherical mirrors
Aperture of lens (mm)	19.54	27
Thickness (mm)	5.27	5
Radius of curvature (mm)	96.54	28.28

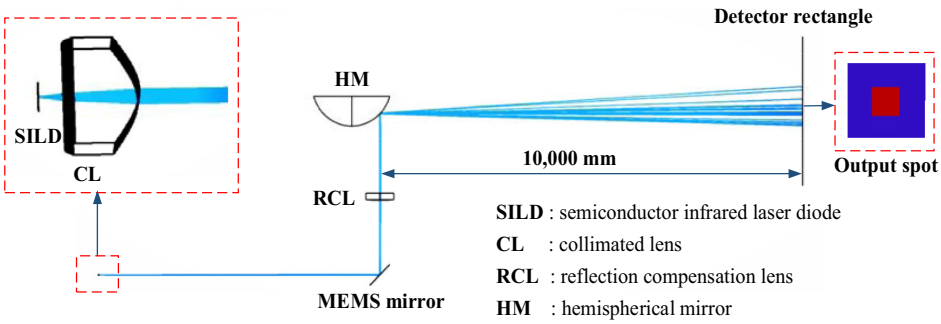

Fig. 7 Simulation of the optical structure of the circum-scanning LiDAR emission optical system in Zemax.

Remarkably, the Gaussian beam produced by the infrared-pulsed laser diode in this system was well collimated after passing through the aspheric lens and the convergent lens, and a rectangular spot with a small size could be detected at a detection distance of 10,000 mm.

3.3 *Analysis and Discussion*

3.3.1 *Analysis of beam collimation*

In the case of detection distances of 100 and 10,000 mm, a rectangular detector received the beam before and after the aspheric lens. In Fig. 8, the sensor displays the pattern of spots it

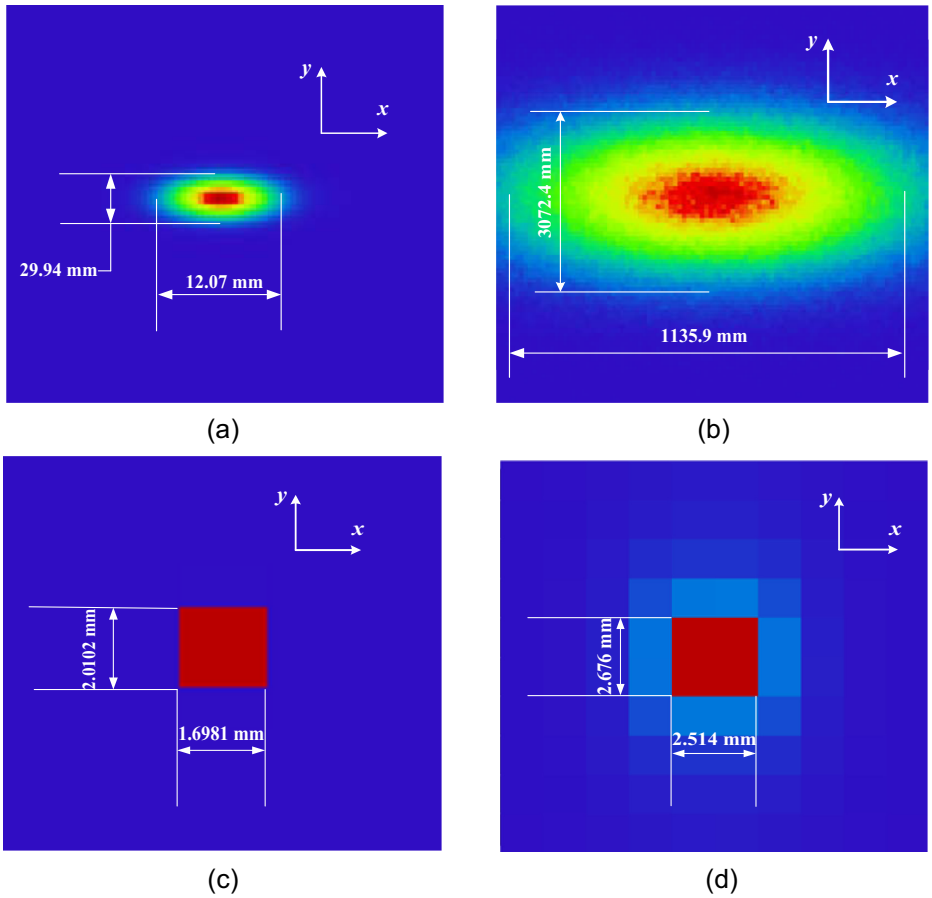

Fig. 8 Comparison of the effect before and after beam collimation: (a) spot size at 100 mm before collimation; (b) spot size at 10,000 mm before collimation; (c) spot size at 100 mm after collimation; and (d) spot size at 10,000 mm after collimation.

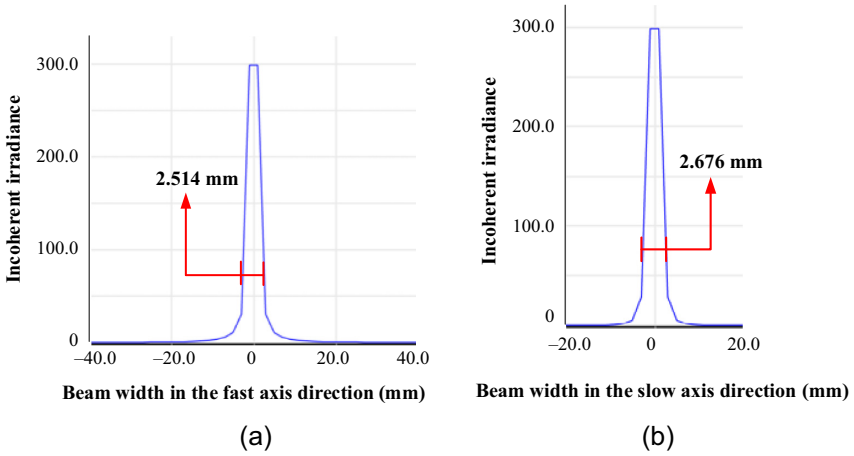

Fig. 9 The relative light intensity distribution of laser diode at 10,000 mm after beam collimation. The relative light intensity distribution of the outgoing beam in the (a) fast-axis direction and (b) slow-axis direction.

received. The spot size at 100 mm without beam alignment is shown in Fig. 8(a); the spot size at 10,000 mm without beam alignment is shown in Fig. 8(b); Fig. 8(c) shows the spot size after collimating the beam at 100 mm; and Fig. 8(d) shows the spot size after collimating the beam at 100 mm. It could be observed that the spot size varied considerably with distance when beam collimation was not carried out. However, with beam collimation, the spot size barely varied with distance. With beam collimation, the spot size at 100 mm was 1.6981 mm in the x direction and 2.0102 mm in the y direction, and at a distance of 10,000 mm, the spot size was 2.514 mm in the x direction and 2.676 mm in the y direction.

According to Fig. 9, we could see the distribution of the relative light intensity after beam collimation. Figure 9(a) shows the relative light intensity distribution of the beam along the fast axis, whereas Fig. 9(b) shows the distribution along the slow axis. At a detection distance of 10,000 mm, the beam became rectangular with a linewidth of <3 mm after collimation with the aspheric lens.

With Zemax, the spot size of the beam in the fast and slow axes before and after collimation was calculated. The rectangular detector was positioned between 100 and 10,000 mm (with an interval of 1000 mm), and the calculation of the spot size was provided in Fig. 10. According to Fig. 10, the left y axis represents the spot before straightening, and the right y axis represents

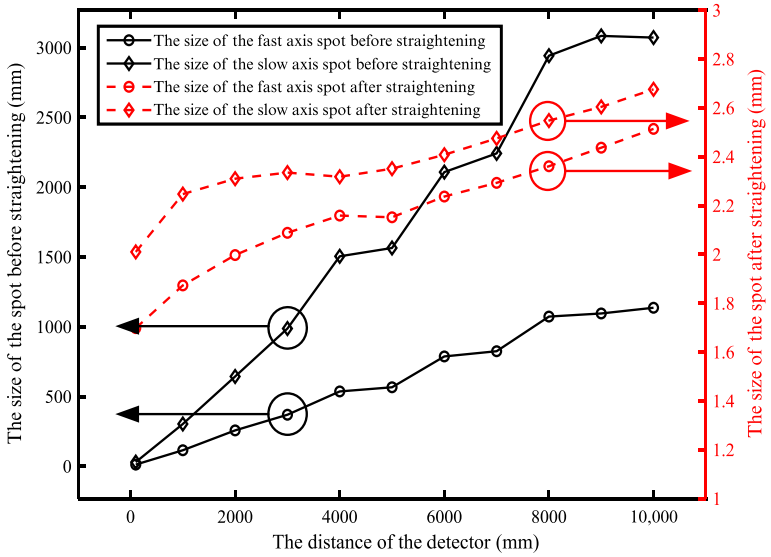

Fig. 10 Variation of spot size at different positions before and after beam collimation.

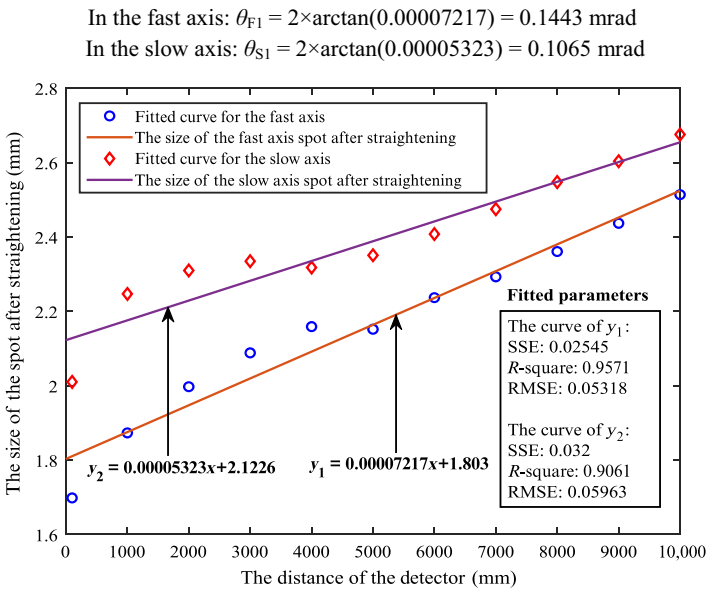

Fig. 11 The fitting curves of spots at different positions after beam collimation in the fast and slow axes.

the spot after straightening. It was observed that the spot size does not change much with distance when collimated, indicating an approximately linear relationship, which shows that the aspheric lens was effective for beam alignment.

The scatter points, which were obtained after the collimation of the aspheric lens at various positions, were fitted to a straight line using MATLAB programming. Figure 11 illustrates the results of curve fitting. Here are the equations for fitting curves: in the fast axis, $y_1 = 0.00007217x + 1.803$; in the slow axis, $y_2 = 0.00005323x + 2.1226$. The error of squares (SSE), *R*-square (R_2), and root mean square error (RMSE) were used as indicators for evaluating the fitting curves in the fast and slow axes, respectively. Here are the evaluation results: in the fast axis, SSE was 0.02545, R_2 was 0.9571, and RMSE was 0.05318; in the slow axis, SSE was 0.032, R_2 was 0.9061, and RMSE was 0.05963. Evaluation results showed a good correlation between the fitting curves and the scatter points.

It was tangent to the half angle of the beam divergence angle after quasistraightness that defined the slope of the fitted curve, which enabled us to calculate the beam divergence angle after collimation. The divergence angle could be calculated as follows:

In the fast axis, $\theta_{F1} = 2 \times \arctan(0.00007217) = 0.1443$ mrad.

In the slow axis, $\theta_{S1} = 2 \times \arctan(0.00005323) = 0.1065$ mrad.

3.3.2 *Analysis of outgoing beam in the system*

As soon as the beam was collimated, it was projected onto the MEMS micromirrors, compensated by the converging lens and then reflected by the spherical mirror and exited. A rectangular detector was used at a detection distance of 10,000 mm to detect the outgoing beams of a spherical mirror. According to Fig. 12, the exit spot produced the following results: Fig. 12(a) indicates the spot size at a detection distance of 10,000 mm in the fast axis. At the same time, Fig. 12(b) shows the spot size at a detection distance of 10,000 mm in the slow axis. The results in this figure illustrate that after the circum-scanning LiDAR emission optical system, the Gaussian beam transformed into rectangular spots with a linewidth of <4 mm.

The spot size of the outgoing beam in the fast and slow axes could be calculated independently with Zemax. The rectangular detector, which was positioned between 100 and 10,000 mm (with an interval of 1000 mm), was used to detect outgoing beams in the system. Using MATLAB programming, spot sizes at different positions were fitted to straight lines. An illustration of the curve-fitting results could be found in Fig. 13. The equations for

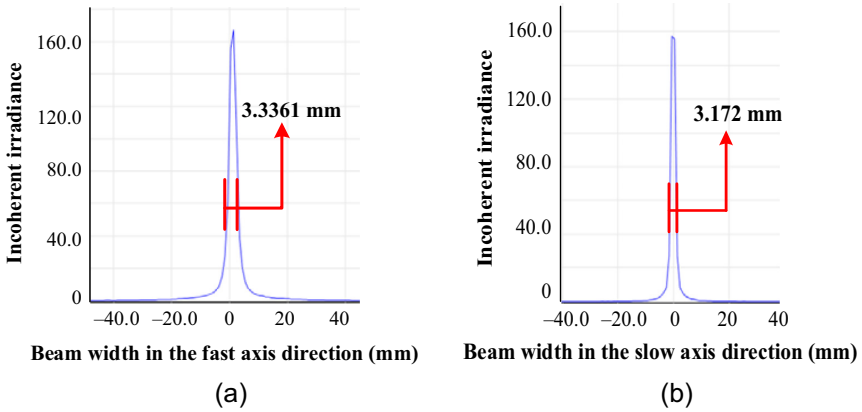

Fig. 12 A diagram illustrating the results of outgoing beam when passing through circum-scanning LiDAR emission optical system. A distribution of relative light intensity along the exit beam at 10,000 mm in the (a) fast axis and (b) slow axis.

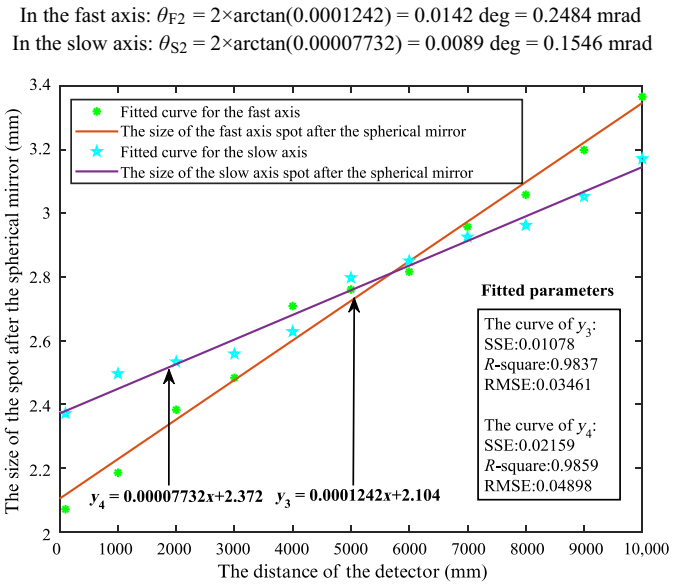

Fig. 13 The fitting curves of spots at different positions after the spherical mirror in the fast and slow axes.

fitting curves were listed: in the fast axis, $y_3 = 0.000142x + 2.104$ and in the slow axis, $y_4 = 0.00007732x + 2.372$. Here are the evaluation results: in the fast axis, SSE was 0.01078, R_2 was 0.9837, and RMSE was 0.03461; in the slow axis, SSE was 0.02159, R_2 was 0.9859, and RMSE was 0.04898.

The tangent defined the slope of the fitted curve to the half-angle of the beam divergence angle after quasistraightness, which allowed us to calculate the divergence angle after the beam was ejected. The divergence angle could be calculated as follows. As a result, we can conclude that the system has a lateral angular resolution of 0.0142 deg:

In the fast axis, $\theta_{F2} = 2 \times \arctan(0.0001242) = 0.0142 \text{ deg} = 0.2484 \text{ mrad}$.

In the slow axis, $\theta_{S2} = 2 \times \arctan(0.00007732) = 0.0089 \text{ deg} = 0.1546 \text{ mrad}$.

According to Eq. (14), the energy utilization of the system η can be calculated, where P represents the incident beam's total energy, and Po is defined as the outgoing beam's total energy. There was 63.12 W of the total energy released from the system exit beam in Zemax, with the distance of the detector set at 10,000 mm. Based on the formula below,

Table 4 Comparison of performance parameters of LiDAR systems studied by different scholars.

Reference	Wavelength (nm)	Detection accuracy (mm)	The field of view (deg)	Detection distance (m)	Angular resolution (deg)
10	905	—	120	250	0.1
20	658	5	40	10	0.09
21	1550	100	60	20	0.23
22	1550	10	42.24	100	—
This paper	905	5	360	10	0.0142

we obtained an energy utilization rate of 84.16% when the light intensity of the system was 75 W. As intended, this result matched the paper's design objectives

$$\eta = \frac{P_o}{P}. \tag{14}$$

This paper compared the circum-scanning LiDAR emission optical system with similar systems designed by others. Table 4 presents the comparison results according to the performance parameters of the divergence angle in the fast and slow axes, the field of view, the detection distance, and the angular resolution.[10,20–22] Data comparison showed that the system designed in this paper had a large scanning angle, good collimation, and high angular resolution.

3.4 *Tolerance Analysis*

Due to processing, assembly and adjustment, and improper handling of the staff, an optical system will exhibit a certain amount of error during the actual production process. Thus tolerance analysis is an important method of assessing optical system stability. A tolerance assignment table for the circum-scanning LiDAR emission system is shown in Table 5.

Based on sensitivity and Monte Carlo analysis methods, a tolerance analysis was conducted using the RMS Y radius as a measure of system performance in this study. As shown in Fig. 14, the tolerance analysis results are displayed as probabilities for changing the angular resolution of the system. The results indicate that 90% of the samples in the circum-scanning LiDAR emission system have angular resolutions below 0.0187 deg. There is no problem with the tolerance range as it meets the angular resolution requirements of the system.

Table 5 Tolerance assignment table for the circum-scanning LiDAR emission system.

Parameter	Specification
Radius of the surface (mm)	±0.002
Conic of the surface	±0.05
Thickness (mm)	±0.005
Surface XY decenter (mm)	±0.01
Surface XY title (deg)	±0.1
Aperture of lens (mm)	±0.005
Index	0.001

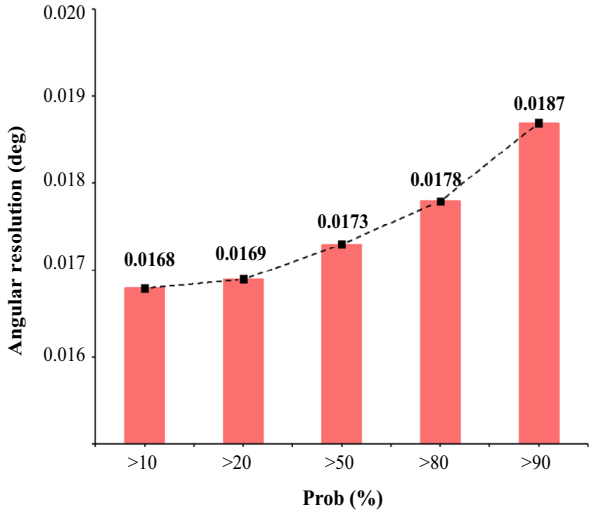

Fig. 14 Tolerance analysis results for the circum-scanning LiDAR emission system.

4 Conclusion

This paper presented a circum-scanning LiDAR emission optical system to overcome the limitations of traditional LiDAR in terms of scanning angle, structure, and resolution and meet miniaturization requirements. Various components made up the system, including the light source, the aspheric lens, the rotating scanning micromirrors, the convergent lens, and the sphere mirror. The aspheric lenses ensured that the outgoing beam was collimated correctly. With the new rotating scanning MEMS micromirrors, the beam projected onto its surface was transformed into a concentric circle. The convergent lens compensated for the divergence of the outgoing beam caused by the spherical mirror. The system was simple, compact, and has a high angular resolution, which made it superior to similar systems and kept up with the future development trends for LiDAR. A circum-scanning LiDAR emission optical system was then designed by ray tracing in Zemax. The fast-axis divergence angle was 0.2484 mrad, the slow-axis divergence angle was 0.1546 mrad, and the system energy utilization rate was 84.16% with an angular resolution of 0.0142 deg. This system, characterized by simple structure and easy fabrication, has extensive applications in 3D scanning imaging LiDAR.

Acknowledgments

This work was supported by the China Postdoctoral Science Foundation (Grant No. 2022M712493), the Natural Science Basis Research Plan in Shaanxi Province of China (Grant No. 2022JQ-676), and the Scientific Research Program of Shaanxi Provincial Education Department (Grant No. 21JY017).

References

1. J. Yunshan et al., "Time-stretch LiDAR as a spectrally scanned time-of-flight ranging camera," *Nat. Photonics* **14**(1), 14–18 (2020).
2. Anonymous, "LiDAR drives forwards," *Nat. Photonics* **12**(8), 441 (2018).
3. T. Raj et al., "A survey on LiDAR scanning mechanisms," *Electronics* **9**(5), 741 (2020).
4. P. An et al., "LiDAR-camera system extrinsic calibration by establishing virtual point correspondences from pseudo calibration objects," *Opt. Express* **28**(12), 18261–18282 (2020).
5. F. Xu et al., "Fast synchronization method of comb-actuated MEMS mirror pair for LiDAR application," *Micromachines* **12**(11), 1292 (2021).
6. M. P. Edgar et al., "Real-time computational photon-counting LiDAR," *Opt. Eng.* **57**(3), 031304 (2018).

7. L. Yunxi et al., "The effect of closed-loop optimization enhances the MEMS LiDAR for rapid scanning," *Optik* **208**, 164097 (2020).
8. C. Niclass et al., "Design and characterization of a 256 × 64-pixel single-photon image in CMOS for a MEMS-based laser scanning time-of-flight sensor," *Opt. Express* **20**(11), 11863–11881 (2012).
9. X. Lee et al., "Optical design of a new folding scanning system in MEMS-based LiDAR," *Opt. Laser Technol.* **125**, 106013 (2020).
10. T. Gies et al., "2D MEMS scanning for LIDAR with sub-Nyquist sampling, electronics, and measurement procedure," *Proc. SPIE* **9495**, 94050F (2015).
11. Z. Hongbo et al., "The conversion from a Gaussian-like beam to a flat-top beam in the laser hardening processing using a fiber coupled diode laser source," *Opt. Laser Technol.* **125**, 106028 (2012).
12. S. Haiyin, "Simple mathematical model for designing laser diode focusing optics with a large numerical aperture," *Opt. Eng.* **53**(10), 105105 (2014).
13. I.-B. Sohn et al., "Laser assisted fabrication of micro-lens array and characterization of their beam shaping property," *Appl. Surf. Sci.* **479**(6), 375–385 (2019).
14. C.-M. Tsai and C.-K. Wu, "Freeform lens design of beam shaping with user-defined rotation-symmetric profile by using numerical method," *IEEE Photonics J.* **11**(3), 1502812 (2019).
15. W. Qu, H. Gu, and Q. Tan, "Design of refractive/diffractive hybrid optical elements for beam shaping with large diffraction pattern," *Chin. Opt. Lett.* **14**(3), 031404 (2016).
16. B. D. Price et al., "Sub-terahertz refractive flat-top beam shaping via 3D printed aspheric lens combination," *Appl. Opt.* **59**(18), 5429–5436 (2020).
17. H. Wu et al., "Beam shaping used to improve the power efficiency of a two-Cassegrain-telescope configuration optical system," *Opt. Lasers Eng.* **28**, 223–231 (2014).
18. O. P. Agrawal, "Generalized variational problems and Euler–Lagrange equations," *Comput. Math. Appl.* **59**(5), 1852–1864 (2010).
19. L. Yang et al., "Freeform optical design of beam shaping systems with variable illumination properties," *Opt. Express* **29**(20), 31993–32005 (2021).
20. K. Kimoto et al., "Development of small size 3D LIDAR," in *Proc. IEEE Int. Conf. Robot. and Automat.*, IEEE Press, pp. 4620–4626 (2014).
21. B. L. Stann et al., "MEMS-scanned ladar sensor for small ground robots," *Proc. SPIE* **7684**, 76841E (2010).
22. X. Lee et al., "Optical design for uniform scanning in MEMS-based 3D imaging LiDAR," *Appl. Opt.* **54**(9), 2219–2223 (2015).

Naitao Xu received his BE degree in microelectronics from the University of Electronic Science and Technology of China in 2006. He has been a philosophic doctor in optical engineering at Xi'an Technological University, Shaanxi Province, China, since 2019. His current research interests include MEMS 3D camera and MEMS LiDAR based on micromirrors chip.

Biographies of the other authors are not available.